The invasion pore induced by *Toxoplasma gondii*

Kegawa Y.,[1*] Male F.[2*], Jiménez-Munguía I.,[1] Blank P.S.,[1] Mekhedov E.,[1] Ward G.,[2**] Zimmerberg J.[1**]

[1] Section on Integrative Biophysics; Division of Basic and Translational Biophysics, *Eunice Kennedy Shriver* National Institute of Child Health and Human Development (NICHD), National Institutes of Health (NIH)

[2] Department of Microbiology and Molecular Genetics, University of Vermont Larner College of Medicine, Burlington, United States.

[*]Contributed equally [**]Corresponding Authors

Abstract

To survive, obligate intracellular apicomplexan parasites must invade host cells. For *Toxoplasma gondii*, a first indication of invasion is a transient breach in host cell permeability that precedes parasite entry. Here, a time-series analysis using novel filtering algorithms was performed on new electrophysiological data acquired at sub-200 μs time resolution. The analysis revealed an underlying structure to the parasite-induced conductance changes: conductance changes are consistent with a rapid insertion, then slower removal, blocking, or inactivation of quantal conductance elements. This quantal element was best described by a Gaussian distribution with mean of 0.26 nS (width 0.03 nS), which is like the conductance of another apicomplexan protein translocon, EXP2. The quantal conductance observed during interactions with parasites depleted of the rhoptry neck protein RON2, a central component of the moving junction between the parasite and the host cell during invasion, had a different Gaussian distribution (mean 0.19 nS, width 0.03 nS) supporting the hypothesis that RON2 contributes to the poration process or the passage of conductive elements through the pore.

INTRODUCTION

Protozoan pathogens belonging to the phylum Apicomplexa cause life-threatening diseases such as malaria, toxoplasmosis, and cryptosporidiosis in humans and other

animals that are important global health burdens with few effective vaccines and limited drugs for treatment (Smith et al., 2021, Striepen, 2013, WHO, 2023). They are obligate intracellular parasites; the intracellular stage of their life cycles begins after host cell invasion. To invade, two types of secretory organelles unique to Apicomplexa are employed: micronemes and rhoptries (Bullen et al., 2019, Carruthers & Sibley, 1997, Dubremetz, 2007, Reviewed in Cova et al., 2022). These organelles contain proteins whose highly coordinated secretion is essential to successful invasion. In *Toxoplasma gondii* (*T. gondii*) tachyzoites, the life cycle stage associated with acute infection, micronemes are abundant organelles mostly located around the parasite's apical pole (Carruthers & Sibley, 1999). The rhoptries are the largest secretory organelles in the tachyzoite and consist of a rhoptry neck and bulb (Counihan et al., 2013, Proellocks et al., 2010). Between the apical tip of the rhoptry and the parasite plasma membrane lies a small apical vesicle (AV). Current understanding of rhoptry secretion involves fusion of the rhoptry with the AV and fusion of the AV with the parasite plasma membrane, resulting in rhoptry exocytosis (Aquilini et al., 2021, Mageswaran et al., 2021, Sparvoli et al., 2022).

One of the most enigmatic of the molecular events during *T. gondii* invasion is the appearance of rhoptry proteins in the host cell cytoplasm even without complete invasion (Koshy et al., 2012, Lamarque et al., 2014). The presence of rhoptry proteins in the host cell cytoplasm seems to violate a fundamental cell biological law governing conservation of membrane and secretory protein topology, i.e. that protein domains co-translationally inserted into the lumen of the ER remain lumenal throughout the secretory pathway, including within secretory granules and, once released from those granules, face the extracellular space. Accordingly, the lumen of the rhoptry is topologically equivalent to the extracellular space and not the host cell cytoplasm. Proteins released from the lumen of the rhoptry can change their topology only by traversing a limiting membrane such as the plasma membrane. The rhoptry neck protein RON2 presents a particularly unique challenge, in that RON2 is a transmembrane protein that is somehow inserted into the host cell plasma membrane after exocytosis, where it both forms the core of a complex of translocated proteins necessary for parasite internalization and serves as a ligand to which receptors in the

Toxoplasma plasma membrane bind (Besteiro et al., 2009, Lamarque et al., 2011, Srinivasan et al., 2011, Lamarque et al., 2014).

Prior to the invasion of the *Toxoplasma* tachyzoite into host cells a transient increase in host cell membrane conductance was identified using time-resolved imaging and electrophysiology (Suss-Toby et al., 1996). Since the transient increase in conductance preceded parasite internalization, the conductance change likely represents an initial host cell membrane modification by the parasite during invasion. In a companion paper (Male and Kegawa et al., 2024) the transient increase in membrane conductance is shown to depend on rhoptry exocytosis although the nature of the perforating agent released from the rhoptries or activated by rhoptry exocytosis remains unknown. Here, a detailed electrophysiological analysis of the conductance transient reveals the presence of multiple stepwise changes in conductance throughout its growth and shrinkage, consistent with a multiple-pore formation model in the host cell membrane. The calculated quantal conductances caused by wild-type or RON2-depleted parasites differ, suggesting a potential role for RON2 in the formation of the inserted pores, or a regulation of their occupancy by cargo. Based on these results, we propose the formation of an "invasion pore" during parasite invasion that may function in rhoptry protein transport into host cell cytoplasm.

MATERIAL AND METHODS

Culture of fibroblast-like COS1 cells

Fibroblast-like COS1 cells (ATCC CRL-1650) were cultured in complete Dulbecco's modified Eagle's medium (DMEM supplemented with high glucose, 200 mM Glutamax, 1 mM sodium pyruvate, ThermoFisher Scientific, Cat#10569, Waltham, MA) with 10% Fetal Bovine Serum Premium Select (R&D Systems, Cat#S11550, Minneapolis, MN) and primocin 100 μg/mL (InvivoGen, Cat# ant-pm-2, San Diego, CA) at 37°C under 5% CO_2. Cells were rinsed twice with DPBS without both $CaCl_2$ and $MgCl_2$ (ThermoFisher Scientific, Cat#14190, Waltham, MA). Cells were released from the flask using a 5-minute incubation with 0.25% trypsin containing 0.913 mM EDTA (GIBCO, Cat#25200-056, Waltham, MA). Trypsinized cells were centrifuged at 193 *x g*, 5 min, room temperature (RT), in complete DMEM, using an Allegra X-22R

centrifuge with Beckman Coulter rotor. Cells were resuspended in complete medium and 1 mL containing 40,000 cells was seeded onto a 35 mm DT dish (Bioptechs, Butler, PA) for 60 minutes at 37°C under 5% CO_2. Before starting electrophysiology experiments, DMEM medium was replaced by live cell imaging solution (LCIS) containing 155 mM NaCl, 3 mM KCl, 2 mM $CaCl_2$, 1 mM $MgCl_2$, 3 mM NaH_2PO_4, 10 mM HEPES, and 20 mM Glucose (final pH 7.4) or low-calcium LCIS containing 155 mM NaCl, 3 mM KCl, 0.1 mM $CaCl_2$, 2.9 mM $MgCl_2$, 3 mM NaH_2PO_4, 10 mM HEPES, and 20 mM Glucose (final pH 7.4).

Culture of human foreskin fibroblasts (HFFs)

HFFs were maintained in Dulbecco's Modified Eagle Medium (DMEM) (Life Technologies, Carlsbad, CA) with 10% v/v heat-inactivated fetal bovine serum (FBS) (Life Technologies, Carlsbad, CA), 10 mM HEPES pH 7.0, 50 U/mL Penicillin-Streptomycin (Thermo Fisher Scientific, Cat#15140122, Waltham, MA) and 25 μg/mL gentamicin (GIBCO, Cat#15750, Waltham, MA). Prior to parasite passage, HFF medium was replaced with fresh culture medium (DMEM containing 10% v/v heat-inactivated FBS, 10 mM HEPES pH 7.0, 50 U/mL Penicillin-Streptomycin.

***Toxoplasma gondii* culture and isolation**

T. gondii RH (hereafter designated WT) and KD-RON2 (Lamarque et al., 2014) strains were passaged in human foreskin fibroblasts (HFFs) (ATCC CRL-1634) grown in DMEM supplemented with 10% heat inactivated FBS (R&D Systems, Cat#S11550, Minneapolis, MN), 50 U/mL Penicillin-Streptomycin (Thermo Fisher Scientific, Cat#15140122, Waltham, MA), and 25 μg/mL gentamicin (GIBCO, Cat#15750, Waltham, MA) at 37°C under 5% CO_2. *Toxoplasma* tachyzoites were isolated from infected monolayers at the large vacuole stage. Freshly released tachyzoites were removed and discarded before collecting infected cells from the culture flask by replacing culture medium with 4 mL of Endo buffer containing 89.4 mM KOH, 44.7 mM H_2SO_4, 10 mM $MgSO_4$, 106 mM sucrose, 5 mM glucose, 20 mM Tris-H_2SO_4, and 3.5 mg/mL BSA (final pH 8.20, adjusted using KOH) (Endo et al., 1987). Attached cells and parasites were collected by scraping and resuspended in Endo solution. Collected infected cells were passed three times through a 25G needle and filtered

through a 5-μm cellulose acetate filter (Sartorius, Cat#S7594-FMOSK, Göttingen, Germany). Isolated parasites were washed three times with Endo solution using a 10 min centrifugation at 400 *x g* and resuspended in 50 μL Endo solution for electrophysiological experiments. Parasites were used within two hours following isolation and were protected from light exposure.

Calcium transient assay

T. gondii culture and isolation

For calcium transient experiments, "untreated" KD-RON2 parasites were grown in medium containing 0.07% ethanol for 48 hours prior to experiments for consistency with all other untreated controls reported in (Male and Kegawa et al., 2024). Isolated parasites were resuspended in anti-SAG1 antibody (monoclonal antibody DG52, a generous gift from Dr. David Sibley, 1/20 dilution of a 0.2 mg/mL stock) conjugated to AlexaFluor 647 (Alexa Fluor™ 647 Antibody Labeling Kit; Molecular Probes, Eugene, OR) in Endo buffer for 30 minutes at RT, then centrifuged at 1000×*g* for 2 minutes, and resuspended in Endo buffer at 3×10^7 parasites/mL.

Cell labeling

HFFs were seeded in 3 chambers of an ibidi μ-Slide VI 0.4 (ibidi GmbH, Gräfelfing, Germany) for 2 hours at 37°C (with 5% CO_2 and humidity) before indicator loading with 5 μM Fluo-4 AM (Invitrogen, Waltham, MA) with 1% PowerLoad Concentrate, 100X (Invitrogen, Waltham, MA) in LCIS for 90 minutes at RT.

Imaging and data analysis

Experiments were carried out at 35-36°C. Fluo-4 labeled cells were washed 1× with Endo buffer before allowing anti-SAG1 pre-labeled parasites to settle on the cells for 10 minutes. The buffer was then exchanged with pre-warmed (35-36°C) invasion-permissive LCIS to capture calcium transients and invasion events. Imaging was carried out on a Nikon Eclipse TE300 widefield epifluorescence microscope (Nikon Instruments, Melville, NY) using a 60× PlanApo λ objective (0.22 pixel/μm, NA 1.4). 1020×1020-pixel images were captured using an iXon 885 EMCCD camera (Andor Technology, Belfast, Ireland) set to trigger mode, with exposure time of 39 ms, no

binning, 30 MHz readout frequency, 3.8× conversion gain, and 300 EM gain. Parasite induced perforation of host cells resulting in calcium transients and subsequent invasion events were observed by near-simultaneous excitation of Fluo-4 (490 nm) and AlexaFluor 647 (635 nm) using a pE-4000 LED illumination system (CoolLED, Andover England), through rapid excitation switching triggered by the NIS Elements Illumination Sequence module (Nikon Instruments, Melville, NY). Hardware was driven by NIS Elements v. 5.11 software (Nikon Instruments, Melville, NY). Calcium transient and invasion events were quantified as described elsewhere (Male and Kegawa et al., 2024) across three biological replicates, each consisting of three technical replicates for protein-depleted mutants and three technical replicates for controls, carried out on the same day. One technical replicate from one biological replicate was excluded from subsequent analysis due to poor quality.

Electrophysiology

Electrophysiological experiments were performed with COS1 cells seeded onto a 35 mm DT dish containing LCIS, the external recording solution. Temperature during the experiment was kept at 37°C. The pipette solution for whole cell recordings contained 122 mM KCl, 2 mM $MgCl_2$, 11 mM EGTA, 1 mM $CaCl_2$, 5 mM HEPES (Final pH 7.26, adjusted with KOH). Patch pipettes (~3 MΩ resistance) were fabricated from 1.5-mm thick wall borosilicate glass capillaries (P1000, Sutter Instruments, Novato, CA). Electrophysiological parameters of each patched cell were monitored with an amplifier (AxoPatch200b, Molecular Devices, San Jose, CA) in the voltage clamp mode. The output current was filtered using the internal 100 kHz Lowpass Bessel filter included in the amplifier, and an external 5 kHz low-pass 8-pole Bessel filter (Model 900 CT/9 L8L, Frequency Devices Inc, Haverhill, MA). A -60 mV holding potential was applied to monitor current changes due to interaction of each strain of *Toxoplasma* tachyzoites with COS1 cells. Current was recorded for a maximum of 15 minutes per cell, digitized at 100 μs (Axon Digidata 1550B and its associated software package Axopatch, Molecular Devices, San Jose, CA). Time resolution of <200 μs was empirically measured, matching the expected value determined by the interaction of the external 5 kHz filter and the whole-cell compensation circuitry of the amplifier. Conductance was calculated using Ohm's law adjusted using the mean pipette access

resistance, R_A (n=40, R_A=2.88/0.34 MΩ mean/sem); with our internal and external solutions, the measured reversal potential of the COS1 cells was ~0 mV. Data analysis was performed offline (Clampfit 11.2, Molecular Devices, San Jose, CA and MatLab r2022b, MathWorks, Natick, MA).

Tachyzoite delivery

Delivery pipettes were fabricated from 1.5-mm thick wall borosilicate glass capillaries using a pipette puller (P-80/PC, Sutter Instruments, Novato, CA). Delivery pipette inner diameters ranged from 10 to 20 µm, which was large enough to allow tachyzoites to pass through without damage. Delivery pipettes were bent (< 45°) over the flame of a small lighter to facilitate a vertical and smooth delivery of parasites onto the surface of a target cell. Parasites were delivered adjacent to the patched cell using a microinjector (FemtoJet® 4i, Eppendorf, Cat#5252000021D, Enfield, CT) set at ~5 hPa.

Optical visualization of invasion and image analysis

Imaging was initiated immediately after a stable, whole cell configuration was achieved. Parasite invasion was monitored on an inverted microscope (Axiovert 200, Zeiss, Oberkochen, Germany) equipped with a 63X 1.4 N.A. objective, differential interference contrast (DIC) optics, and a sCMOS camera (12.2 frames per second, 1501M-GE, ThorLab, Newton, NJ). Imaging proceeded for 15 min or until disruption of the giga-ohm seal required for whole cell electrophysiology, whichever occurred first. Offline, image files were screened for the presence or absence of parasite invasion, identified by DIC as a visible constriction of tachyzoites at the COS1 cell plasma membrane as they entered the cell. The number of parasites delivered onto the cell surface, as well as the number of invasions were counted to determine a ratio of invasion events per parasite.

Data analysis for the electrophysiological recordings

Electrophysiological data was processed using MatLab. Digitized data were converted into a current and voltage data array using abfload (Hentschke, v1.4.0.0, MatLab Central File Exchange). Conductance and current plots were generated from the raw

data following median filtering. MatLab median filter function, medfit1, was applied to remove noise spikes from the raw data to facilitate identification of biologically relevant transients. The choice of the median filter (9 points) was established empirically, balancing rejection of noise spikes, with minimal reduction in the amplitude of the parasite-induced transient. Typically, the noise spikes are significantly shorter than biologically relevant spikes with typical durations ~ 0.4 ms. To identify the biologically relevant transients several criteria were used, including changes in the moving variance, first derivative, and manual inspection. The hand-curated selection of data was implemented in MatLab scripts to extract the transients. To identify transient and peak conductance starting and ending times, sequence change point analysis (MatLab findchangepts) was used to identify the times of mean conductance changes that persisted longer than 10 ms or 100 samples (100 μs each). Change point analysis identifies a change in signal statistics with time, for example the mean, of the whole cell conductance signal. As the number of change points existing in the conductance data was unknown, a range of fixed values were added to the residual error (a penalty term linear with the number of change points to compensate for the decrease in residual error that each additional change point introduced), until a plateau in the residual error was observed. The change point parameter set associated with stabilizing the residual error was used to calculate global features of the conductance transient: peak and residual conductance magnitudes, time to reach both the peak and residual conductance, and transient and peak duration. The peak is calculated from the magnitude of the maximum changepoint conductance value while the peak duration is the difference in time between the two change points defining the peak conductance. The transient duration is calculated from the difference between the first and last change points. The residual conductance is the difference between the mean of the last 50 ms and the mean of the first 95 ms in the 1 sec time series capturing each transient, where the first detected change in conductance for each spike is set at 100 ms. Time to reach the peak conductance is defined by the time between the start of the transient and the start of the maximum change point mean statistic and the time to reach the residual conductance is defined by the time between the end of the maximum change point mean and the last change point. Modeling the total resistance as the sum of the pore

($R_{pore} = \frac{\rho * L}{\pi * r^2}$) and twice the pore access ($R_{access} = \frac{\rho}{4 * r}$) resistances, calculation of the radius (r) of a cylindrical pore (length L, solution resistivity ρ) with maximum conductance G_{max} of each transient is

$$r = \left(G_{max} * \frac{\rho}{4}\right) * (1 + \left(1 + \frac{4^2 * L}{G * \rho * \pi}\right)^{0.5})$$

Statistical analyses

Comparisons between the global features of the conductance transients observed in WT and KD-RON2 (peak and residual conductance, and transient duration) were evaluated using one-way analysis of variance (ANOVA) following both tests for normality (Lilliefors Test) and homogeneity of variance (Levene's Test). The residual conductance distributions were not normal, displaying long-tails; one-way ANOVA of Box-Cox transformed data was used following the removal of one negative value in the KD-RON2 data set. To validate comparisons relying on distributional assumptions (one-way ANOVA), the bootstrap with 1,000,000 replicates was used to calculate 95% confidence intervals (CIs) at an alpha level of 0.05 for differences between data set means. CIs bracketing zero were consistent with no evidence for a significant difference between data sets. Rise and falling time distributions were compared using the two-sample Kolmogorov-Smirnov test. Rejection of the null hypothesis was set at $p < 0.05$ for ANOVA, Lilliefors, Levene's, and Kolmogorov-Smirnov tests.

Two mixture model approaches were used to analyze distributions of data to provide a robust assessment: 1) fitting the empirical cumulative distribution function (eCDF) to a parametric model consisting of a weighted sum of normal or log-normal distributions and 2) applying a Gaussian mixture distribution model using both supervised (MatLab GMModel, iterative expectation maximization) and unsupervised (Wallace and Dowe, 2000 as coded by Statovic V 0.81, minimum message length) clustering algorithms. Graphs showing 95% confidence interval shadings were prepared using the Gramm data visualization toolbox for MatLab (V 2.27.1 by Pierre Morel). All statistical tests were two-sided unless indicated otherwise.

Determination of clustered conductance values

Piece wise constant (PWC) filtering was used to analyze the time dependent conductance changes observed during a transient (Little & Jones, 2011; implemented in MatLab using pwc_cluster.m). PWC filtering is an unsupervised cluster analysis amenable to one-dimensional times series that optimizes membership within identified conductance levels (clusters). PWC filtering preserves sharp boundaries and other characteristics of rapid transitions ('jumps') in the data, and it does not require that the number of clusters be specified because the analysis is unsupervised. Here, a conductance level or state is hypothesized to be PWC with variable magnitude and duration depending upon the number and lifetime of individual conductance units present. Like change point analysis, removing noise from PWC signals is a signal processing optimization problem with many established iterative procedures. Here PWC filtering was applied using a clustering algorithm where each data point is shifted towards the highest density (mean-shift) within a fixed distance centered at the data point (hard kernel) (Little & Jones, 2011). In addition, the number of uniquely sized conductance levels following optimization is related to the amount of filtering and is set by an additional parameter called a 'tuning hyperparameter'. Since the amount of filtering can be adjusted using this tuning hyperparameter, the PWC conductance levels are sensitive to the magnitude of this parameter, and there is a risk of fitting the noise if the parameter is too small. To avoid fitting the noise, an optimization procedure that identified the noise level of the baseline was adopted. The ~100 ms baseline prior to the start of a transient (as above, it is set by us at 100 ms) was assumed to represent a PWC signal with noise properties associated with the whole cell configuration and that the noise present in the baseline is present and constant for the duration of the transient. The minimum constant conductance level change identified using the PWC filtering was set to be greater than the 99% confidence interval of the noise present in the constant baseline. The tuning hyperparameter was iteratively adjusted over a range until the resulting level changes were greater than the minimum constant conductance level change identified in the baseline noise. The hyperparameter satisfying the constraint defined by the baseline noise was considered optimal filtering for the transient. Since the noise varied between

experiments, the resulting level changes were pooled from individually processed conductance transients.

Testing for quantal conductance changes using the differences between adjacent clustered values

The magnitude of the level changes, obtained by calculating the absolute value of the differences between identified PWC levels present in the conductance transient time series, constitute the data sets whose distributional properties were analyzed as described above. To create the set of level changes, the PWC representation of the conductance time series was numerically differentiated by taking first order differences between the time series (t_i-$t_{(i-1)}$). Zero differences were dropped; only the positive and negative changes between conductance levels were analyzed. These changes represent the 'jumps' between levels at the specified time where the filtering defined a change in the cluster set associated with the new level. Except for sign, the positive and negative level changes had symmetric and equal distributions, justifying working with the absolute values of the level changes. If the distribution of level changes was uniform across all possible conductance differences (all possible conductance steps are represented in the data set), then there would be no evidence for a dominant peak or mode. However, if the distribution has one or more well defined peaks, then these peaks can be analyzed as a weighted sum of individual Gaussian distributions using mixture models to identify the peak with the greatest contribution to the overall distribution. Distributional peaks were visualized using a non-parametric density approximation prior to Gaussian mixture model analysis for identification and statistical evaluation of the peak properties, as described above.

RESULTS

Each invading wild-type *T. gondii* tachyzoite produces an individual conductance transient.

We previously reported a large transient conductance increase prior to the invasion of *T. gondii* tachyzoites (Suss-Toby et al., 1996). In the current study, transients were collected with the *T. gondii* wild-type (WT) RH strain using high bandwidth direct current measurements of host cells (COS1) under voltage-clamp conditions in the

whole-cell configuration. Simultaneously, parasite invasion was monitored by DIC microscopy (Figure 1a). Multiple parasites were delivered to the host cells to increase the probability of capturing multiple invasions and the associated transient increases in whole-cell current. Invading tachyzoites showed a clear constriction (arrowheads, Figure 1a) and a single large current change was detected prior to the constriction of each parasite: multiple transients were recorded when multiple parasites invaded the same host cell (Figure 1b). Parasite invasion (*i.e.*, visible constriction) and the current transient were correlated events; no instance of invasion was observed without a transient (16 invasions with 16 transients). However, transients were sometimes detected without parasite invasion (9/25 WT transients). Further analysis was performed on all the transients identified using the WT strain (n=25). The analysis revealed that every transient possessed characteristic wave form features – a fast rise to the peak and a slower fall to a new baseline – although the magnitude and duration of the transients varied (*e.g.,* Figure 1c and Supplementary Figure 1).

The transient conductance increase induced by wild-type parasites occurs independently of complete moving junction formation.

The depletion of rhoptry neck protein 2 (RON2) leads to a severe early invasion defect wherein rhoptry proteins are seen inside the host cell but the parasite subsequently detaches (Lamarque et al., 2014). There is no evidence of moving junction formation when a RON2-deficient parasite attaches to a host cell, but we cannot rule out the formation of a partial or incomplete moving junction lacking the RON2/AMA1 binding partners. Since RON2 is the only component of the complete moving junction that is inserted as a transmembrane protein in the host cell plasma membrane, it was reasonable to hypothesize that RON2 contributes to the properties of host cell perforation. To investigate whether RON2 insertion (and thus complete moving junction formation) are associated with the appearance of transients, we used both current recording experiments and the calcium influx assay (Male and Kegawa et al., 2024) to interrogate the ability of RON2 knockdown (KD-RON2) parasites to generate the conductance and calcium transients independently. KD-RON2 parasites express undetectable levels of RON2, even without the ATc treatment typically used to induce knockdown, and show a severe invasion defect (Lamarque et al.,2014). While zero

out of 159 KD-RON2 parasites invaded COS1 cells in our electrophysiology experiments, *i.e.,* no visible constrictions were observed by DIC microscopy, 19.5% (13.7%-26.5%; lower-upper 95% CI) of the same parasites generated conductance transients (Figure 2). Similar results were seen using the calcium transient assay (Figure 2). The ability of the KD-RON2 parasites to generate conductance and calcium transients at levels similar to WT parasites stands in contrast to the near absence of calcium transients seen when the parasites are depleted of proteins regulating rhoptry exocytosis (Male and Kegawa et al., 2024). Together, the conductance and calcium transient results indicate that neither RON2 insertion into the host cell plasma membrane nor complete moving junction formation are required for induction of the transient increase in the host cell plasma membrane conductance.

Detailed analysis of conductance transients induced by WT and KD-RON2 parasites.

The transients produced by both the WT (n=25) and KD-RON2 parasites (n=31; hereafter in this paper we will refer to untreated KD-RON2 as simply KD-RON2 unless otherwise noted) were averaged and compared (Supplementary Figure 2 and Figure 3a). On average, both WT and KD-RON2 parasite conductance transients show a rapid increase and slower decrease in conductance during the transient. To further characterize and compare the transients, change point analysis of individual transients was performed (Figure 3b). Individual transients are described by four characteristic features (mean±std. dev.) for WT and KD-RON2 (n=25 and n=31, respectively): 1) Peak conductance, calculated as the difference in conductance between the baseline and the maximum change point mean (WT: 3.40±1.12 nS and KD-RON2: 3.01±1.40 nS, Figure 3c); 2) Residual conductance, calculated as the difference in conductance between the pre- and post-transient baselines (WT: 0.54±0.38 nS and KD-RON2: 0.39±0.33 nS, Figure 3d); 3) Transient duration, calculated as the time between transient initiation and the beginning of residual conductance (WT: 322±219 ms and KD-RON2: 374±203 ms, Figure 3e), and 4) Peak conductance duration, calculated as the difference in the starting and ending changepoint time of the maximum conductance identified (WT: 73±64 ms and KD-RON2: 118±86 ms, Figure 3f). Both the WT and KD-RON2 transient waveforms begin

with a rapid increase in conductance, reaching a maximum value with exponentially distributed time constants of 50±10 ms and 51±9 ms (mean±std. err.; n=25 and n=31), followed by exponentially distributed decreases (fall times) to the residual conductance with time constants of 197±39 ms and 203±36 ms (mean+/-std. err.; n=25 and n=31). For any one parasite strain (WT or KD-RON2), the rise time and fall time distributions are significantly different from each other; two-sample Kolmogorov-Smirnov test, p_{WT}=3.97E-04 and $p_{KD\text{-}RON2}$=8.08E-4; n=25 and n=31, respectively). Comparing the two strains, there is no evidence for differences between WT and KD-RON2 peak conductance, residual mean conductance, or mean transient duration. However, between WT and KD-RON2 strains the peak conductance duration is different (Figure 3f). The change point analysis supports the hypothesis that the kinetic process for creating and removing the conductance pathway for WT and KD-RON2 are similar (rise and fall time distributions, peak conductance, and transient duration: Figure 3c-e) but the lifetime (peak duration: Figure 3f) of the maximal conductance state is significantly longer in the absence of RON2.

Step-like transients induced by WT and KD-RON2 parasites differ in quantal conductance.

The above parameterization of the transients was consistent with similar pores produced by WT and KD-RON2 parasites, but what biological mechanism explains the longer peak conductance duration observed in the averaged transients and confirmed in the analysis of the individual peak durations (Figure 3a and 3f)? This question led us to investigate the transient dataset at higher temporal resolution, which revealed that individual transients display rapid changes in conductance levels in both the rising and falling phases of the transients. Further examination of the transient waveform was performed to analyze the magnitudes and numbers of the rapid, step-like changes in conductance. Each transient was processed using PWC denoising as described in methods and the distributions of conductance level changes were calculated (Figure 4a). The cumulative distribution of conductance level changes was first fit non-parametrically and the resulting fit was used to generate a density distribution of conductance level differences. WT parasite-induced transients display a density peak at 0.26 nS, which supports the hypothesis of a characteristic, quantal

conductance increment or step size (Figure 4b and 4c). Both parametric model fitting, and Gaussian mixture modeling identified a primary Gaussian peak at 0.26 nS with a width of 0.03 nS. When the same analysis was applied to the KD-RON2 conductance transients, a primary Gaussian peak at 0.19 nS with a width of 0.03 nS was identified (Figure 4b and 4c). The KD-RON2 primary conductance density peak is 30% lower than that observed in WT. The means of the WT and KD-RON2 Gaussian peaks (0.26 and 0.19 nS, respectively) were interpreted as quantal values associated with the conductance changes observed in the transient wave form. Transforming the individual conductance transients demonstrated that the number of quantal units contributing to the maximum conductance for both parasite lines are approximated by Poisson distributions with parameters 13.08 and 15.90 for WT and KD-RON2, respectively. There is no evidence for a difference in the number of quantal units contributing to the conductance maximum observed in WT and KD-RON2 transients (bootstrap differences in the Poisson parameter, alpha=0.05, Supplementary Figure 3a and 3b).

DISCUSSION

The distinctive transient increase in host cell membrane conductance detected after parasite attachment but preceding the morphological changes of invasion implies that for a brief time ions can freely move across the host cell membrane. Most likely, this is due to the appearance in the host cell membrane of an aqueous pathway for ion flux, either due to protein-lined channels or a local breakdown of the lipid bilayer. The transient proceeds along a series of intermediates in conductance: once initiated, the conductance rises in tens of milliseconds, reaching a peak before diminishing more slowly to a residual conductance that is by one second after onset approximately 10% of the peak. Neither RON2 nor by extension the establishment of the RON2-AMA1 complex were required for the transient increase of either membrane conductance or Ca^{2+} entry. Also consistent with an aqueous pathway for ion flux (also known as a "pore") is the proportionality of Ca^{2+} flux into the host cell cytoplasm during a transient with extracellular Ca^{2+} concentration, as shown in our companion paper, where it was also shown that transients require rhoptry exocytosis (Male and Kegawa et al., 2024). However, extracellular calcium is not itself likely to be the

charge-carrying ion or required for either pore opening or closing, since conductance transients of similar shape and magnitude were observed in an environment with twenty times lower extracellular calcium concentration (Supplementary Figure 4). Based on these combined data, we propose that the conductance and calcium transients we have observed are manifestations of a rhoptry exocytosis-dependent host cell membrane poration process during invasion (see Figure 7, Male and Kegawa et al., 2024). What follows are deductions based on analysis of the electrophysiological data on this poration process and the development of the current working hypothesis (termed invasion pores, Figure 5).

Kinetics of the conductance transient do not match one single large channel opening and closing.

The tight association between the transient conductance increase and parasite invasion, and the observation that the transient always precedes the first invasion-associated morphological changes in the parasite suggests that the transient plays an important role in invasion. Here we consider molecular structures that might underly the transient. The initial analysis of the data revealed that the average transient durations, peak conductance, and residual conductance were indistinguishable between WT and KD-RON2 parasites. This suggests that the underlying molecular structures for the transients are robust. The time dependence of the conductance change is not consistent with a simple model of one on/off channel opening and closing, which predicts one step increase in conductance followed by a step decrease of the same size. Not only are the recordings visually different from this prediction, but the transient relaxes to a residual conductance greater than the initial baseline, followed by a more variable time to return to baseline. Even if a single pore could be tuned with sub-conductance states to reflect the data, the properties of such a pore would not correlate to a porosome-like structure, 40 – 50 nm in diameter, that was previously observed by electron microscopy on the membrane over the conoid (Dubremetz, 2007). Using a simple model to convert the peak conductance of the transients observed in our study to the diameter of a single cylindrical pore yields diameters of only 3 - 10 nm (Supplementary Figure 5). Furthermore, the fast and transient conductance changes reported in this study

reflect a dynamic transition of the pore size, suggesting it would be challenging to capture the observed pore size using static images. If a cylindrical pore 40 - 50 nm in diameter were to form, the membrane conductance would be ~34 - ~44 nS and not 1 - 6 nS.

Multiple pores open and close in the host cell membrane during the invasion of Toxoplasma.

The characteristics of the transient obtained from the high-resolution analysis suggest that multiple poration events occur to increase the permeability of the host cell membrane after rhoptry exocytosis and independent of moving junction formation. Detailed analysis of transients revealed a fast increase in the conductance with a slower decay composed of multiple "steps in conductance" identified by change point analysis (Figure 3a). Multiple steps in conductance are not unusual for proteinaceous pores having sub-conductance states, such as the voltage-dependent anion channel from Neurospora or rat liver (Zimmerberg and Parsegian, 1986). The largest component in the distribution of conductance step sizes for VDAC is the main open-closed transition (also ~ 0.25 nS in salt solutions close to those used here). Importantly, in the current study, the largest conductance component is different between WT (0.26 nS) and KD-RON2 (0.19 nS) parasites. This difference could result from RON2 either being directly involved in the structure of the invasion pore or regulating its formation. The lack of significant differences in the peak and residual conductance magnitudes, time to reach both the peak and the residual conductance, and the transient duration of individual spikes (other than the duration of the maximal conductance level) indicates pore formation itself is likely independent of RON2 [irrespective of any residual RON2, see Lamarque et al., 2014]. If the lack of a wild-type moving junction allows more ion diffusion across it, we would expect to report larger quantal values, not lower, so that is ruled out; conversely if a moving junction lacking RON2 is more occluding to ion diffusion, this could explain these results. Among rhoptry neck proteins, RON2 is a transmembrane protein that could contribute to increasing membrane conductance via membrane insertion. Also, if RON2 insertion is the direct cause of poration or if RON2 regulates pore opening, then the rise time of the transient would likely be different between WT and KD-RON2. However, there

is no support for significant differences between WT and KD-RON2 when comparing their rise time or fall time distributions. An alternative explanation for the difference in the distribution of step size between WT and KD-RON2 parasites is that depletion of RON2 modifies which rhoptry proteins pass through the pore, how they pass, or their local concentration near the invasion pore. Any of these factors could have an indirect impact on how ions flow through the pore. In fact, besides the absence of RON2, KD-RON2 parasites abnormally localize other rhoptry neck proteins, such as RON4 and RON5 (Lamarque et al., 2014). These proteins, usually localized in the rhoptry neck, do not localize to the rhoptries in the absence of RON2. If the pore is the entry pathway into the host cell for rhoptry proteins such as the RONs and ROPs, trafficking of rhoptry proteins through the pore could impact the magnitude of the conductance increment: the smaller quantal conductance for KD-RON2 could be a consequence of rhoptry proteins that linger in the invasion pore and occlude ion flow. This would also explain the longer residence time of the KD-RON2 pore, indicated by the maximal conductance duration (Figure 3f). This result is understandable if the function of the invasion pore is related to the passage of rhoptry cargo through the pore: longer times are needed to move cargo through a smaller pore, and once the cargo has passed through, the invasion pore is no longer needed. As documented above, the rising and falling phases are kinetically and distributionally indistinguishable for both WT and KD-RON2 transients, suggesting a RON2-*independent* insertion and removal process coupled to a RON2-*dependent* process that influences the lifetime of the maximal conductance state.

Known apicomplexan pores and translocons.

If the pores described here function in rhoptry protein translocation, they may share features with other known protein translocons. In this study, the conductance transient induced during invasion is best fit by quantal increments of ~260 pS, strikingly like the single channel values obtained by direct measurement for the pore-forming protein EXP2 (Garten et al., 2018), a critical component of the well-studied PTEX translocon in malaria parasites (de Koning-Ward et al., 2009, Kalanon et al., 2016). PTEX functions to export proteins across the PVM and into host red blood cell cytoplasm. The membrane conductance of EXP2 was measured using an on-vacuole

patch clamp method, yielding a functional channel conductance of ~190 - 300 pS (Garten et al., 2018).

In *T. gondii*, few pore-forming proteins or potential translocons have been identified. The PVM-associated Myr protein complex functions after invasion in the translocation of secreted dense granule proteins across the PVM into the host cell cytosol (Franco et al., 2016, Cygan et al., 2020). Dense granule proteins GRA17, GRA23, GRA47 and GRA72 are pore-forming proteins that also appear to function post-invasion in nutrient transport across the PVM (Gold et al., 2015, Bitew et al., 2024), although a role for these proteins in protein translocation across the PVM cannot be ruled out. Intriguingly, *Plasmodium* EXP2 is able to rescue loss-of-function phenotypes in *Toxoplasma* lacking GRA17 (Gold et al., 2015). *Toxoplasma* also encodes two perforin-like proteins, TgPLP1 and TgPLP2. PLP2 is only expressed in the sexual stages (Kafsack et al., 2009) but PLP1 forms pores in the PVM and host cell membrane during tachyzoite egress from the host cell (Roiko & Carruthers, 2013). PLP1 pore-forming activity is pH-dependent, with higher activity in acidic compared to neutral conditions (Roiko & Carruthers, 2013). Invasion assays conducted in low pH conditions result in increased levels of parasite attachment and invasion, due to increased microneme secretion, and also increased levels of host cell wounding, potentially due to PLP1 (Roiko & Carruthers, 2013). Based on the structure of PLP1 (Ni et al., 2018), it seems unlikely it can function as a protein translocon.

The mechanism underlying the rapid closure of the invasion pore reported here is also a mysterious phenomenon. To prevent host cell death, invasion-dependent breaches in host cell plasma membrane barrier function are typically rapidly sealed. Closing of the pores may reflect 1) a host cell response to repair the sudden change in permeability through rapid endocytosis (Corrotte et al., 2020), 2) blebbing of the plasma membrane to remove the pores following their insertion, as observed in cell membrane repair studies (Jimenez et al., 2014), or 3) gated closure of the invasion pore once cargo is delivered. The existence of residual conductance implies that the invasion pore is not completely closed and remains in the host cell membrane during the invasion process, which takes a total of 15-20 sec. Further studies are required to identify the essential molecules, decipher the structures involved in pore formation and closure, and understand their biological functions.

Conclusions.

In this study we describe a transient permeability pathway in the host cell membrane during *Toxoplasma* invasion. The electrophysiology data are best explained by synchronous creation of multiple pores by material secreted from the rhoptries into the host cell plasma membrane (Figure 5). We hypothesize that this poration creates a pathway for delivery of secreted rhoptry proteins into the host cell cytoplasm. Because the delivery of these proteins is required for successful parasite invasion, we propose to use the term 'invasion pore' to describe this hypothesis. Further studies are needed to test the invasion pore hypothesis, and to identify the exact molecule(s) that form the pore and initiate its opening and closing.

Figure legends

Figure 1. Each invading *T. gondii* WT RH strain tachyzoite produces a single electrical transient. a) DIC microscopy of Toxoplasma invasion of a COS1 cell under visible patch pipette (left center, upper panel); 10-μm scale bar. Four parasites (P1-P4) invaded during recording of a whole-cell patch-clamp electrophysiology experiment. White arrowheads indicate visible constrictions observed when parasites penetrate the host cell during invasion (middle panel: P1 and P2 invasions; lower panel: P3 and P4 invasions; 3-μm scale bar panels P1-P4). b) Multiple transients were detected from the electrophysiological recording obtained under the whole-cell configuration (-60 mV holding potential) during the invasions of the four parasites. c) Expanded time record of the transients (T1-T4) shown in b) for a clearer visualization of the wave form.

Figure 2. *T. gondii* invasion pore formation does not require RON2, and thus does not require complete moving junction formation. Phenotype of untreated WT and KD-RON2 parasites evaluated using electrophysiology (G) or calcium assay (Ca^{2+}) data sets. Percentages of conductance and calcium transients (% of n parasites presented to host cells). Errors are Wilson, two-tailed upper and lower 95% confidence intervals. The percentage of transients observed in KD-RON2 (G) and KD-RON2 (Ca^{2+}) are not significantly different from WT (G) (two-proportion z-test, z=0.8389, 1.227, p=0.40, 0.22, respectively).

Figure 3. The conductance transients induced by WT and KD-RON2 tachyzoites differ in peak duration but not in transient duration nor peak or residual conductance. a) Conductance waveforms for WT (blue) and KD-RON2 strains (red) (mean, solid lines; 95% CI, shadings; n=25, 31, respectively). b) Representative change point analysis (CPA) of a transient waveform induced by a WT parasite. Time dependent changes in conductance are represented by the gray continuous line over a selected duration of 1 second. Characteristic features of the transient are highlighted in the box. c-f). Violin plots comparing the waveform parameters obtained for WT and KD-RON2 parasites: c) peak conductance, d) residual conductance, e) transient duration, and f) peak conductance duration. Note, in 3f the peak durations are different; bootstrap

differences in the mean, alpha=0.05; ANOVA, p=0.034 without Box-Cox transformation; following Box-Cox transformation and Welch's T-test for unequal variance, p=5.69E-17.

Figure 4. Evidence for quantal conductance levels from time series analysis of individual transient recordings. a) Piece wise constant (PWC) filtering was used to analyze the time-dependent conductance changes observed during individual transients. Examples of three WT-induced transients analyzed using PWC filtering to calculate the distributions of conductance level changes. b) Cumulative distribution function of combined transient conductance level changes (ΔLevel G) produced by WT and KD-RON2 strains (n=25, 30; black and red, respectively) . c) Density distribution of the same data presented in b).

Figure 5. Model for invasion pore formation during parasite invasion. Invasion pore formation is triggered by rhoptry exocytosis (see companion paper, Male and Kegawa et al., 2024). Electrophysiological analysis supports multiple rather than single pore formation on the host cell membrane. Pore formation occurs prior to moving junction formation, but differences in the dominant quantal values induced by WT and KD-RON2 parasites suggest that RON2 contributes to the poration process or the passage of rhoptry contents through the pore.

Supplementary Figure 1. Gallery of 25 WT parasite conductance transients calculated from recorded current measured using -60 mV holding potential.

Supplementary Figure 2. Gallery of 31 KD-RON2 parasite conductance transients calculated from recorded current measured using -60 mV holding potential.

Supplementary Figure 3. The same number of quantal units contribute to the conductance maxima of WT and KD-RON2 transients. a) Transformation of the mean transient conductance (Figure 3a) using the peak quantal sizes for WT (0.26 nS) and KD-RON2 (0.19 nS), rounded to nearest integer. b) Violin plots of the number of

quantal units at the maximum conductance of WT and KD-RON2 transients (n = 25 and 31, respectively).

Supplementary Figure 4. Transients induced by WT parasites in low external calcium concentration (0.1 mM $CaCl_2$) have similar properties to WT transients induced in regular LCIS (2.0 mM $CaCl_2$; Figure 3a). The average waveform of low-calcium transients displays the characteristic fast rise to peak conductance and slower recovery to a new baseline (n=10).

Supplementary Figure 5. Violin plot of pore diameters calculated from individual WT transient maximum conductance using a model for a cylindrical pore (see methods).

Acknowledgements

Transgenic parasites were kindly gifted from Dr. Maryse Lebrun from Université Montpellier. This work was supported by the intramural program of the NICHD (JZ) and U.S. Public Health Service grant U01AI169067 (GEW). YK was supported in part by a JSPS research fellowship for Japanese Biomedical and Behavioral researchers at NIH from 2021 to 2023.

Author contributions

Experiments were performed by YK, FM, IJM and EM, data analysis PB, YK and FM, conceptualization and writing was conducted by all authors.

References

Aquilini, E., Cova, M. M., Mageswaran, S. K., Dos Santos Pacheco, N., Sparvoli, D., Penarete-Vargas, D. M., Najm, R., Graindorge, A., Suarez, C., Maynadier, M., Berry-Sterkers, L., Urbach, S., Fahy, P. R., Guérin, A. N., Striepen, B., Dubremetz, J. F., Chang, Y. W., Turkewitz, A. P., & Lebrun, M. (2021). An Alveolata secretory machinery adapted to parasite host cell invasion. Nature microbiology, 6(4), 425–434. https://doi.org/10.1038/s41564-020-00854-z

Besteiro, S., Michelin, A., Poncet, J., Dubremetz, J. F., & Lebrun, M. (2009). Export of a Toxoplasma gondii rhoptry neck protein complex at the host cell membrane to form the moving junction during invasion. PLoS pathogens, 5(2), e1000309. https://doi.org/10.1371/journal.ppat.1000309

Bitew, M. A., Gaete, P. S., Swale, C., Maru, P., Contreras, J. E., & Saeij, J. P. J. (2024). Two Toxoplasma gondii putative pore-forming proteins, GRA47 and GRA72, influence small molecule permeability of the parasitophorous vacuole. mBio, 15(3), e0308123. https://doi.org/10.1128/mbio.03081-23

Bullen, H. E., Bisio, H., & Soldati-Favre, D. (2019). The triumvirate of signaling molecules controlling Toxoplasma microneme exocytosis: Cyclic GMP, calcium, and phosphatidic acid. PLoS pathogens, 15(5), e1007670. https://doi.org/10.1371/journal.ppat.1007670

Carruthers, V. B., & Sibley, L. D. (1997). Sequential protein secretion from three distinct organelles of Toxoplasma gondii accompanies invasion of human fibroblasts. European journal of cell biology, 73(2), 114–123.

Carruthers, V. B., & Sibley, L. D. (1999). Mobilization of intracellular calcium stimulates microneme discharge in Toxoplasma gondii. Molecular microbiology, 31(2), 421–428. https://doi.org/10.1046/j.1365-2958.1999.01174.x

Corrotte, M., Cerasoli, M., Maeda, F. Y., & Andrews, N. W. (2020). Endophilin-A2-dependent tubular endocytosis promotes plasma membrane repair and parasite invasion. Journal of cell science, 134(5), jcs249524. https://doi.org/10.1242/jcs.249524

Counihan, N. A., Kalanon, M., Coppel, R. L., & de Koning-Ward, T. F. (2013). Plasmodium rhoptry proteins: why order is important. Trends in parasitology, 29(5), 228–236. https://doi.org/10.1016/j.pt.2013.03.003

Cova, M. M., Lamarque, M. H., & Lebrun, M. (2022). How Apicomplexa Parasites Secrete and Build Their Invasion Machinery. Annual review of microbiology, 76, 619–640. https://doi.org/10.1146/annurev-micro-041320-021425

de Koning-Ward, T. F., Gilson, P. R., Boddey, J. A., Rug, M., Smith, B. J., Papenfuss, A. T., Sanders, P. R., Lundie, R. J., Maier, A. G., Cowman, A. F., & Crabb, B. S. (2009). A newly discovered protein export machine in malaria parasites. Nature, 459(7249), 945–949. https://doi.org/10.1038/nature08104

Cygan, A. M., Theisen, T. C., Mendoza, A. G., Marino, N. D., Panas, M. W., & Boothroyd, J. C. (2020). Coimmunoprecipitation with MYR1 Identifies Three Additional Proteins within the Toxoplasma gondii Parasitophorous Vacuole Required for Translocation of Dense Granule Effectors into Host Cells. mSphere, 5(1), e00858-19. https://doi.org/10.1128/mSphere.00858-19

Dubremetz J. F. (2007). Rhoptries are major players in Toxoplasma gondii invasion and host cell interaction. Cellular microbiology, 9(4), 841–848. https://doi.org/10.1111/j.1462-5822.2007.00909.x

Endo, T., Tokuda, H., Yagita, K., & Koyama, T. (1987). Effects of extracellular potassium on acid release and motility initiation in Toxoplasma gondii. J Protozool, 34(3), 291-295. https://doi:10.1111/j.1550-7408.1987.tb03177.x

Franco, M., Panas, M. W., Marino, N. D., Lee, M. C., Buchholz, K. R., Kelly, F. D., Bednarski, J. J., Sleckman, B. P., Pourmand, N., & Boothroyd, J. C. (2016). A Novel Secreted Protein, MYR1, Is Central to Toxoplasma's Manipulation of Host Cells. mBio, 7(1), e02231-15. https://doi.org/10.1128/mBio.02231-15

Garten, M., Nasamu, A. S., Niles, J. C., Zimmerberg, J., Goldberg, D. E., & Beck, J. R. (2018). EXP2 is a nutrient-permeable channel in the vacuolar membrane of Plasmodium and is essential for protein export via PTEX. Nature microbiology, 3(10), 1090–1098. https://doi.org/10.1038/s41564-018-0222-7

Gold, D. A., Kaplan, A. D., Lis, A., Bett, G. C., Rosowski, E. E., Cirelli, K. M., Bougdour, A., Sidik, S. M., Beck, J. R., Lourido, S., Egea, P. F., Bradley, P. J., Hakimi, M. A., Rasmusson, R. L., & Saeij, J. P. (2015). The Toxoplasma Dense Granule Proteins GRA17 and GRA23 Mediate the Movement of Small Molecules between the Host and the Parasitophorous Vacuole. Cell host & microbe, 17(5), 642–652. https://doi.org/10.1016/j.chom.2015.04.003

Jimenez, A. J., Maiuri, P., Lafaurie-Janvore, J., Divoux, S., Piel, M., & Perez, F. (2014). ESCRT machinery is required for plasma membrane repair. Science (New York, N.Y.), 343(6174), 1247136. https://doi.org/10.1126/science.1247136

Kafsack, B. F., Pena, J. D., Coppens, I., Ravindran, S., Boothroyd, J. C., & Carruthers, V. B. (2009). Rapid membrane disruption by a perforin-like protein facilitates parasite exit from host cells. Science (New York, N.Y.), 323(5913), 530–533. https://doi.org/10.1126/science.1165740

Kalanon, M., Bargieri, D., Sturm, A., Matthews, K., Ghosh, S., Goodman, C. D., Thiberge, S., Mollard, V., McFadden, G. I., Ménard, R., & de Koning-Ward, T. F. (2016). The Plasmodium translocon of exported proteins component EXP2 is critical for establishing a patent malaria infection in mice. Cellular microbiology, 18(3), 399–412. https://doi.org/10.1111/cmi.12520

Koshy, A. A., Dietrich, H. K., Christian, D. A., Melehani, J. H., Shastri, A. J., Hunter, C. A., & Boothroyd, J. C. (2012). Toxoplasma co-opts host cells it does not invade. PLoS pathogens, 8(7), e1002825. https://doi.org/10.1371/journal.ppat.1002825

Lamarque, M., Besteiro, S., Papoin, J., Roques, M., Vulliez-Le Normand, B., Morlon-Guyot, J., Dubremetz, J. F., Fauquenoy, S., Tomavo, S., Faber, B. W., Kocken, C. H., Thomas, A. W., Boulanger, M. J., Bentley, G. A., & Lebrun, M. (2011). The RON2-AMA1 interaction is a critical step in moving junction-dependent invasion by

apicomplexan parasites. PLoS pathogens, 7(2), e1001276. https://doi.org/10.1371/journal.ppat.1001276

Lamarque, M. H., Roques, M., Kong-Hap, M., Tonkin, M. L., Rugarabamu, G., Marq, J. B., Penarete-Vargas, D. M., Boulanger, M. J., Soldati-Favre, D., & Lebrun, M. (2014). Plasticity and redundancy among AMA-RON pairs ensure host cell entry of Toxoplasma parasites. Nature communications, 5, 4098. https://doi.org/10.1038/ncomms5098

Little, M. A., & Jones, N. S. (2011). Generalized methods and solvers for noise removal from piecewise constant signals. II. New methods. Proceedings. Mathematical, physical, and engineering sciences, 467(2135), 3115–3140. https://doi.org/10.1098/rspa.2010.0674

Mageswaran, S. K., Guérin, A., Theveny, L. M., Chen, W. D., Martinez, M., Lebrun, M., Striepen, B., & Chang, Y. W. (2021). In situ ultrastructures of two evolutionarily distant apicomplexan rhoptry secretion systems. Nature communications, 12(1), 4983. https://doi.org/10.1038/s41467-021-25309-9

Male, F., Kegawa, Y., Blank, S. P., Jimenez-Munguia, I., Sidik, M. S., Valleau, D., Lourido, S., Lebrun, M., Zimmerberg, J., & Ward, E. G. (2024). Perforation of the host cell plasma membrane during Toxoplasma gondii invasion requires rhoptry exocytosis. *bioRxiv.*

Ni, T., Williams, S. I., Rezelj, S., Anderluh, G., Harlos, K., Stansfeld, P. J., & Gilbert, R. J. C. (2018). Structures of monomeric and oligomeric forms of the Toxoplasma gondii perforin-like protein 1. Science advances, 4(3), eaaq0762. https://doi.org/10.1126/sciadv.aaq0762

Proellocks, N. I., Coppel, R. L., & Waller, K. L. (2010). Dissecting the apicomplexan rhoptry neck proteins. Trends in parasitology, 26(6), 297–304. https://doi.org/10.1016/j.pt.2010.02.012

Roiko, M. S., & Carruthers, V. B. (2013). Functional dissection of Toxoplasma gondii perforin-like protein 1 reveals a dual domain mode of membrane binding for cytolysis and parasite egress. The Journal of biological chemistry, 288(12), 8712–8725. https://doi.org/10.1074/jbc.M113.450932

Smith, N. C., Goulart, C., Hayward, J. A., Kupz, A., Miller, C. M., & van Dooren, G. G. (2021). Control of human toxoplasmosis. International journal for parasitology, 51(2-3), 95–121. https://doi.org/10.1016/j.ijpara.2020.11.001

Sparvoli, D., Delabre, J., Penarete-Vargas, D. M., Kumar Mageswaran, S., Tsypin, L. M., Heckendorn, J., Theveny, L., Maynadier, M., Mendonça Cova, M., Berry-Sterkers, L., Guérin, A., Dubremetz, J. F., Urbach, S., Striepen, B., Turkewitz, A. P., Chang, Y. W., & Lebrun, M. (2022). An apical membrane complex for triggering rhoptry exocytosis and invasion in Toxoplasma. The EMBO journal, 41(22), e111158. https://doi.org/10.15252/embj.2022111158

Srinivasan, P., Beatty, W. L., Diouf, A., Herrera, R., Ambroggio, X., Moch, J. K., Tyler, J. S., Narum, D. L., Pierce, S. K., Boothroyd, J. C., Haynes, J. D., & Miller, L. H. (2011). Binding of Plasmodium merozoite proteins RON2 and AMA1 triggers commitment to invasion. Proceedings of the National Academy of Sciences of the United States of America, 108(32), 13275–13280. https://doi.org/10.1073/pnas.1110303108

Striepen B. (2013). Parasitic infections: Time to tackle cryptosporidiosis. Nature, 503(7475), 189–191. https://doi.org/10.1038/503189a

Suss-Toby, E., Zimmerberg, J., & Ward, G. E. (1996). Toxoplasma invasion: the parasitophorous vacuole is formed from host cell plasma membrane and pinches off via a fission pore. Proceedings of the National Academy of Sciences of the United States of America, 93(16), 8413–8418. https://doi.org/10.1073/pnas.93.16.8413

World Malaria Report 2023. World Health Organization 2023. https://www.who.int/teams/global-malaria-programme/reports/world-malaria-report-2023.

Zimmerberg, J., & Parsegian, V. A. (1986). Polymer inaccessible volume changes during opening and closing of a voltage-dependent ionic channel. Nature, 323(6083), 36–39. https://doi.org/10.1038/323036a0

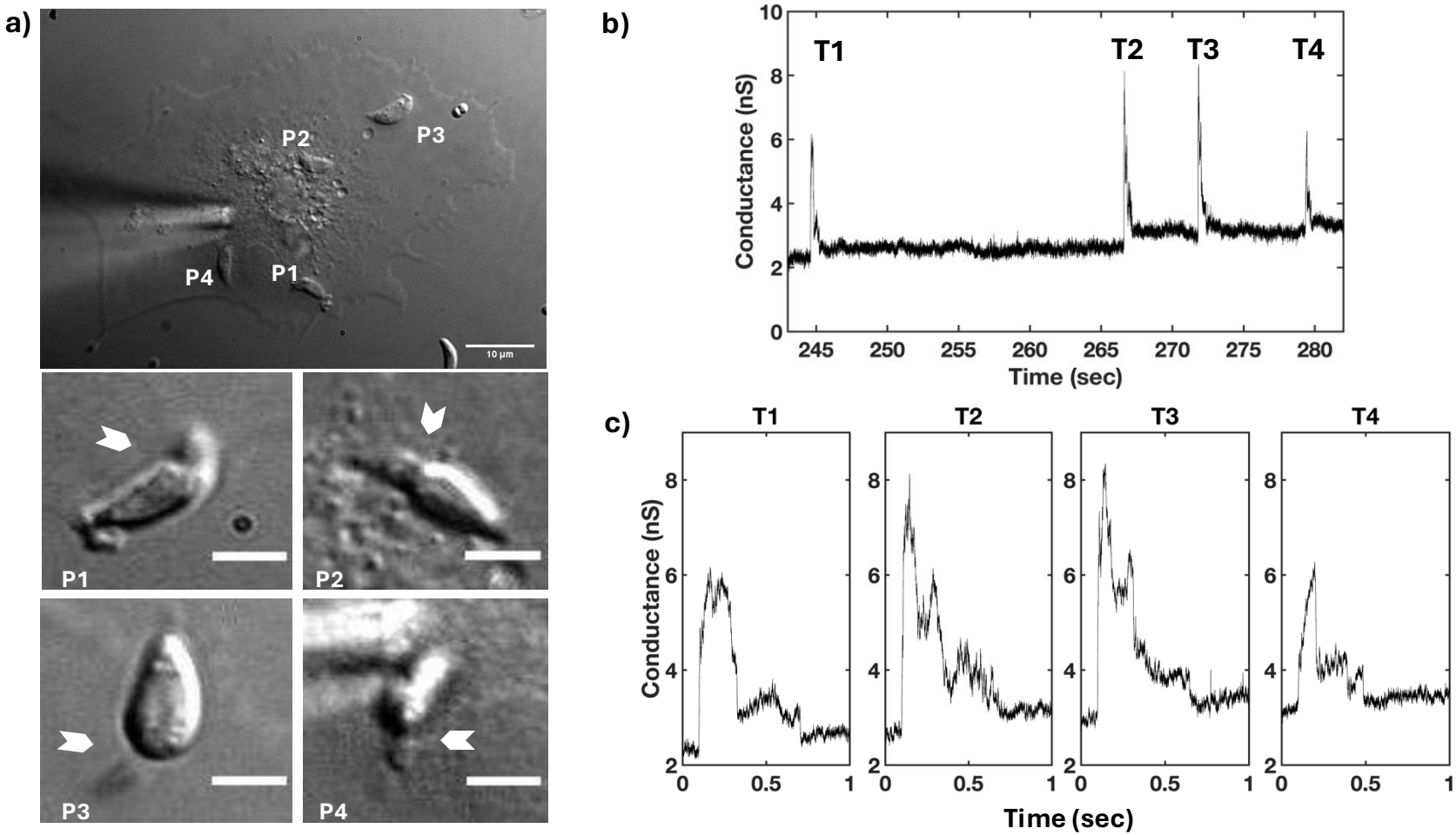

Figure 1. Each invading *T. gondii* WT RH strain tachyzoite produces a single electrical transient. a) DIC microscopy of *Toxoplasma* invasion of COS1 cell under visible patch pipette (left center, upper panel); 10-µm scale bar. Four parasites (P1-P4) invaded during recording of a whole-cell patch-clamp electrophysiology experiment. White arrowheads indicate visible constrictions observed when parasites penetrate the host cell during invasion (middle panel: P1 and P2 invasions; lower panel: P3 and P4 invasions; 3-µm scale bar panels P1-P4). b) Multiple transients were detected from the electrophysiological recording obtained under the whole-cell configuration (-60 mV holding potential) during the invasions of the four parasites. c) Expanded time record of the transients (T1-T4) shown in b) for a clearer visualization of the wave form.

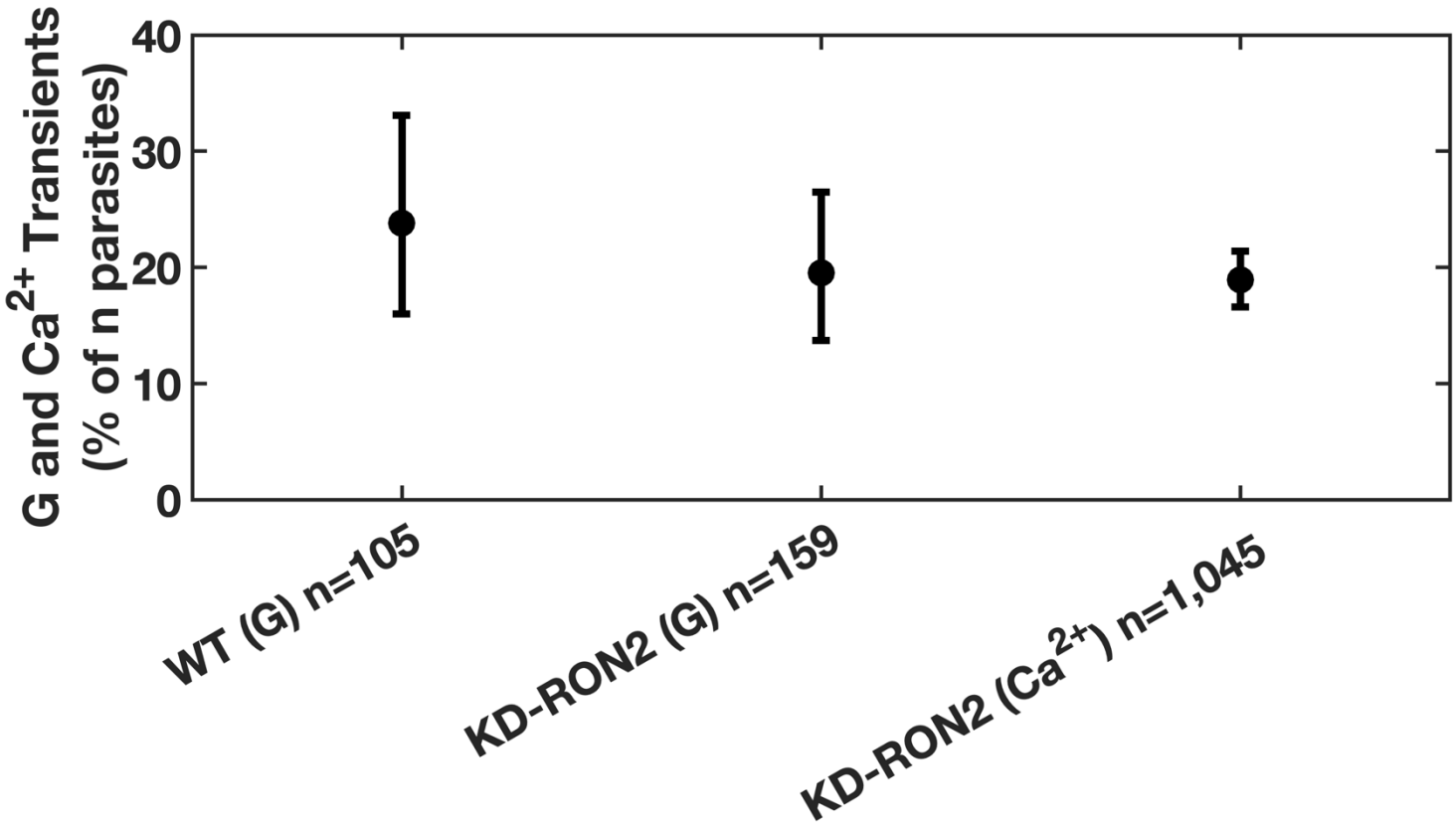

Figure 2. *T. gondii* invasion pore formation does not require RON2, and thus does not require complete moving junction formation. Phenotype of untreated WT and KD-RON2 parasites evaluated using electrophysiology (G) or calcium assay (Ca^{2+}) data sets. Percentages of conductance and calcium transients (% of n parasites presented to host cells). Errors are Wilson, two-tailed upper and lower 95% confidence intervals. The percentage of transients observed in KD-RON2 (G) and KD-RON2 (Ca^{2+}) are not significantly different from WT (G) (two-proportion z-test, z=0.8389, 1.227, p=0.40, 0.22, respectively).

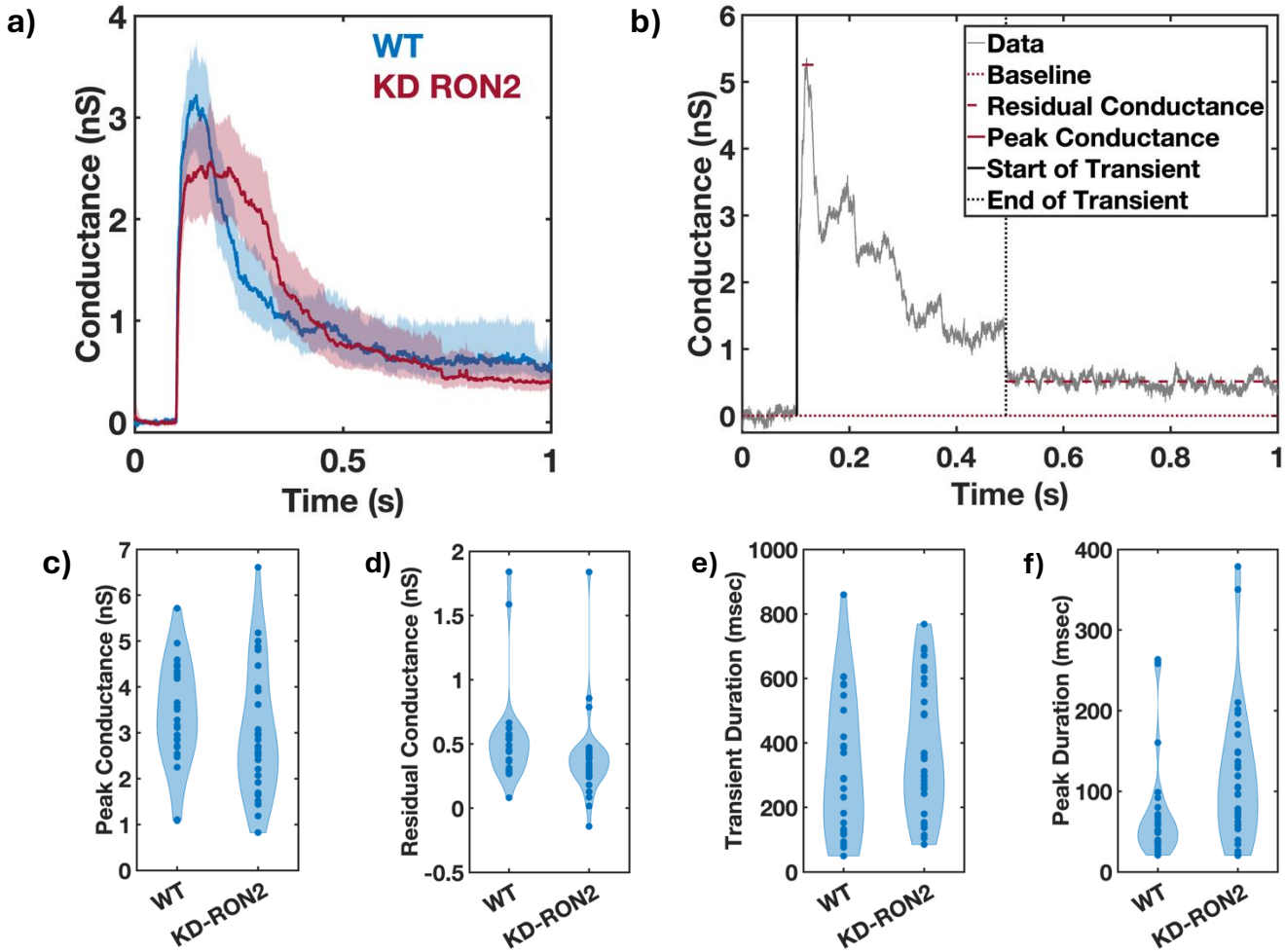

Figure 3. The conductance transients induced by WT and KD-RON2 tachyzoites differ in peak duration but not in transient duration nor peak or residual conductance. a) Conductance waveforms for WT (blue) and KD-RON2 strains (red) (mean, solid lines; 95% CI, shadings; n=25, 31, respectively). b) Representative change point analysis (CPA) of a transient waveform induced by a WT parasite. Time dependent changes in conductance are represented by the gray continuous line over a selected duration of 1 second. Characteristic features of the transient are highlighted in the box. c-f). Violin plots comparing the waveform parameters obtained for WT and KD-RON2 parasites: c) peak conductance, d) residual conductance, e) transient duration, and f) peak conductance duration. Note, in 3f the peak durations are different; bootstrap differences in the mean, alpha=0.05; ANOVA, p=0.034 without Box-Cox transformation; following Box-Cox transformation and Welch's T-test for unequal variance, p=5.69E-17.

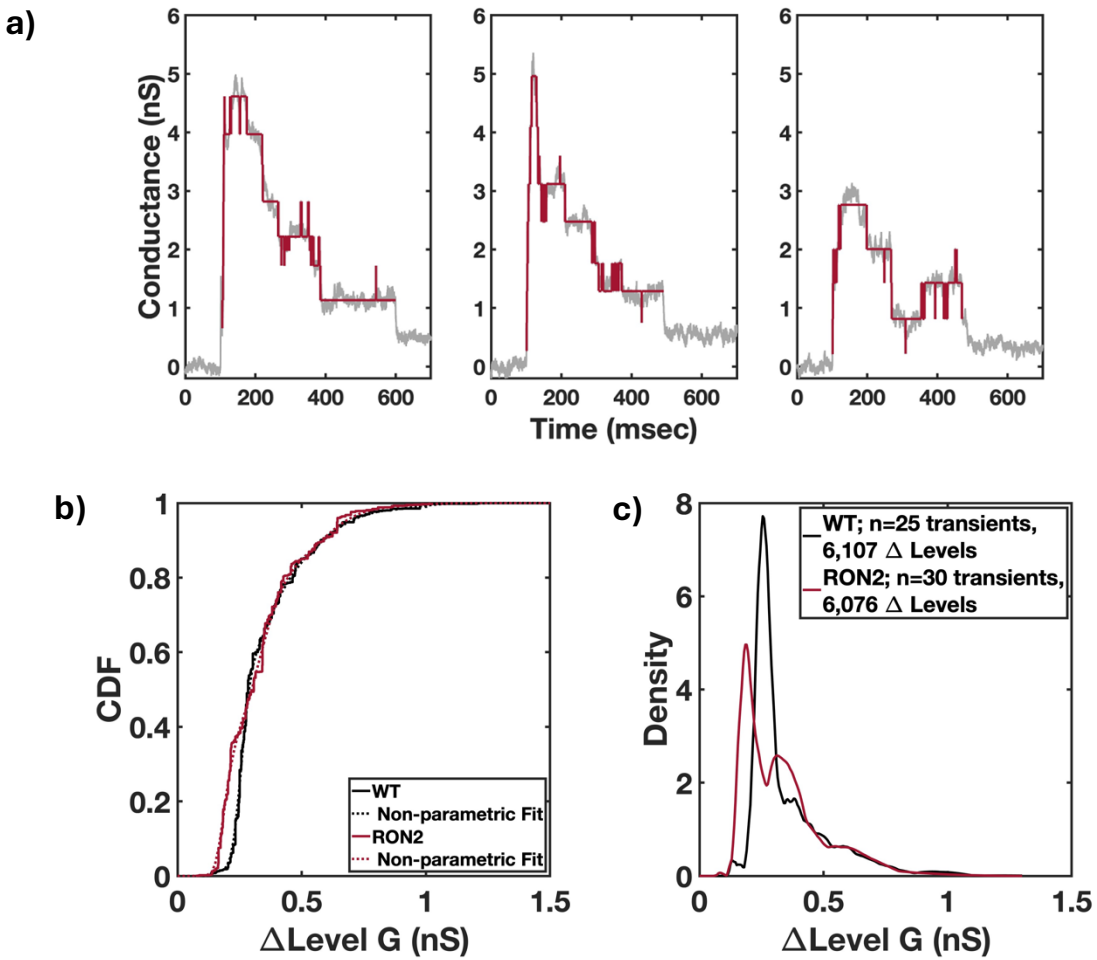

Figure 4. Evidence for quantal conductance levels from time series analysis of individual transient recordings. a) Piece wise constant (PWC) filtering was used to analyze the time-dependent conductance changes observed during individual transients. Examples of three WT-induced transients analyzed using PWC filtering to calculate the distributions of conductance level changes. b) Cumulative distribution function of combined transient conductance level changes (ΔLevel G) produced by WT and KD-RON2 strains (n=25, 30; black and red, respectively) . c) Density distribution of the same data presented in b).

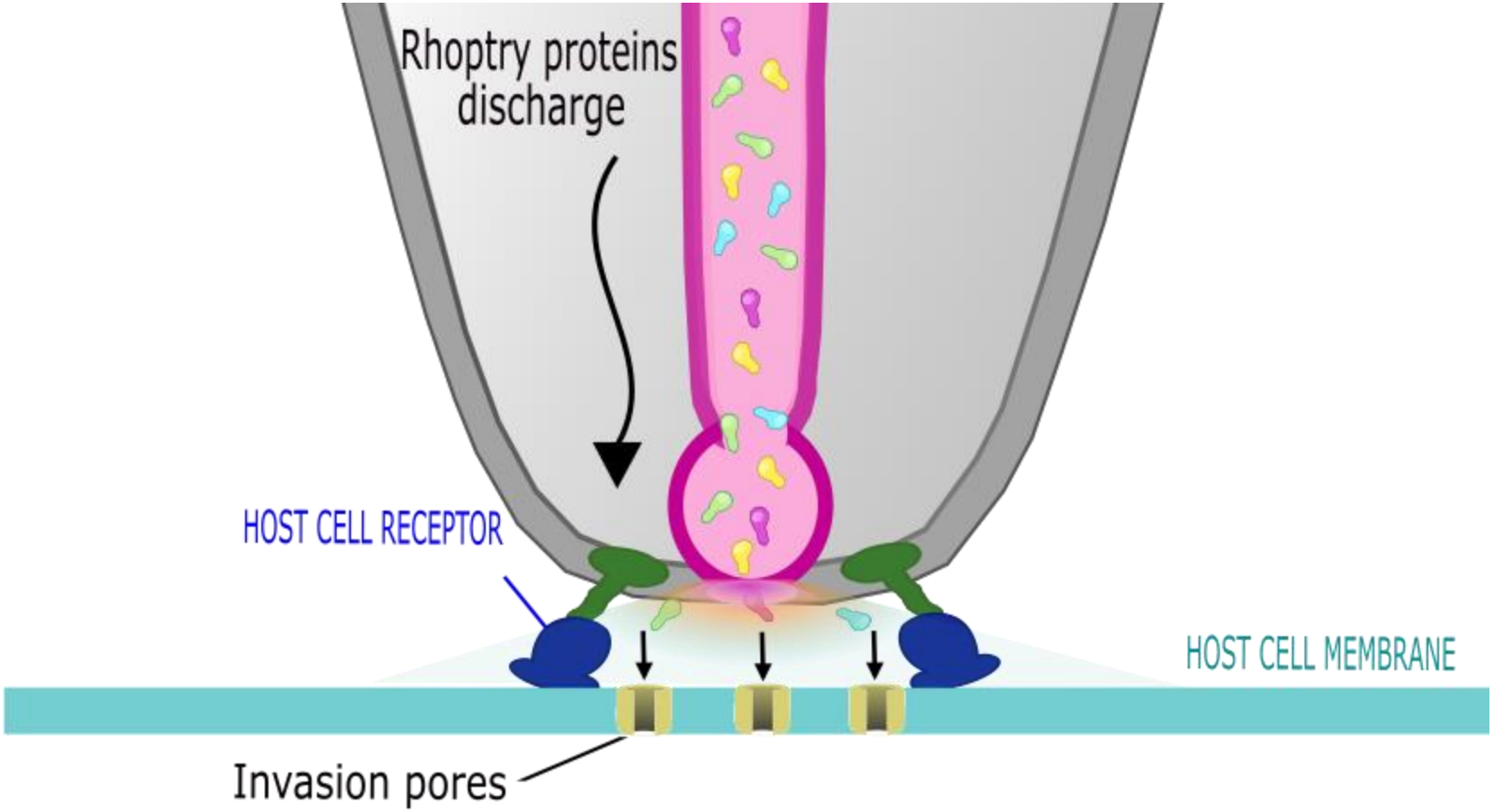

Figure 5. Model for invasion pore formation during parasite invasion. Invasion pore formation is triggered by rhoptry exocytosis (see companion paper, Male and Kegawa et al., 2024). Electrophysiological analysis supports multiple rather than single pore formation on the host cell membrane. Pore formation occurs prior to moving junction formation, but differences in the dominant quantal values induced by WT and KD-RON2 parasites suggest that RON2 contributes to the poration process or the passage of rhoptry contents through the pore.